

This is a repository copy of *Understanding the vibrational structure and ultrafast dynamics of the metal carbonyl pre-catalyst [Mn(ppy)(CO)<sub>4</sub>]*.

White Rose Research Online URL for this paper:

<https://eprints.whiterose.ac.uk/213661/>

Version: Published Version

---

**Article:**

Hunt, Neil Terrence [orcid.org/0000-0001-7400-5152](https://orcid.org/0000-0001-7400-5152), Lynam, Jason Martin [orcid.org/0000-0003-0103-9479](https://orcid.org/0000-0003-0103-9479), Eastwood, Jonathan et al. (1 more author) (2024) Understanding the vibrational structure and ultrafast dynamics of the metal carbonyl pre-catalyst [Mn(ppy)(CO)<sub>4</sub>]. ACS Physical Chemistry Au. ISSN 2694-2445

<https://doi.org/10.1021/acspchemau.4c00037>

---

**Reuse**

This article is distributed under the terms of the Creative Commons Attribution (CC BY) licence. This licence allows you to distribute, remix, tweak, and build upon the work, even commercially, as long as you credit the authors for the original work. More information and the full terms of the licence here:

<https://creativecommons.org/licenses/>

**Takedown**

If you consider content in White Rose Research Online to be in breach of UK law, please notify us by emailing [eprints@whiterose.ac.uk](mailto:eprints@whiterose.ac.uk) including the URL of the record and the reason for the withdrawal request.

# Understanding the Vibrational Structure and Ultrafast Dynamics of the Metal Carbonyl Precatalyst $[\text{Mn}(\text{ppy})(\text{CO})_4]$

Published as part of ACS Physical Chemistry Au virtual special issue "Ultrafast Spectroscopy of Chemical Transformations."

Jonathan B. Eastwood, Barbara Procacci, Sabina Gurung, Jason M. Lynam,\* and Neil T. Hunt\*

Cite This: <https://doi.org/10.1021/acspchemau.4c00037>

Read Online

ACCESS |

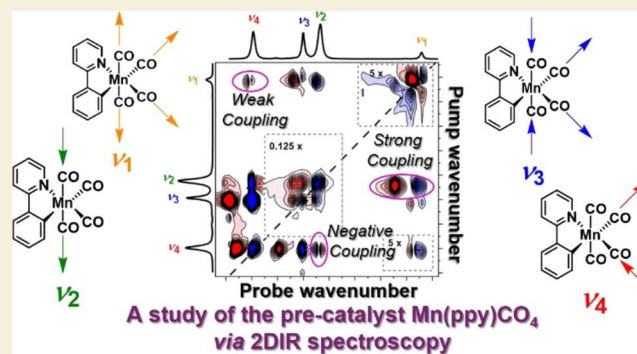
Metrics & More

Article Recommendations

Supporting Information

**ABSTRACT:** The solution phase structure, vibrational spectroscopy, and ultrafast relaxation dynamics of the precatalyst species  $[\text{Mn}(\text{ppy})(\text{CO})_4]$  (**1**) in solution have been investigated using ultrafast two-dimensional infrared (2D-IR) spectroscopy. By comparing 2D-IR data with the results of anharmonic density functional theory (DFT) calculations, we establish an excellent agreement between measured and predicted inter-mode couplings of the carbonyl stretching vibrational modes of **1** that relates to the atomic displacements of axial and equatorial ligands in the modes and the nature of the molecular orbitals involved in M–CO bonding. Measurements of IR pump–probe spectra and 2D-IR spectra as a function of waiting time reveal the presence of ultrafast (few ps) intramolecular vibrational energy redistribution between carbonyl stretching modes prior to vibrational relaxation. The vibrational relaxation times of the CO-stretching modes of **1** are found to be relatively solvent-insensitive, suggestive of limited solvent–solute interactions in the ground electronic state. Overall, these data provide a detailed picture of the complex potential energy surface, bonding and vibrational dynamics of **1**, establishing a fundamental basis for the next steps in understanding and modulating precatalyst behavior.

**KEYWORDS:** ultrafast spectroscopy, 2D-IR spectroscopy, homogeneous catalysis, manganese-catalyzed C–H bond activation, solvent–solute interaction



## INTRODUCTION

Transition-metal carbonyl complexes play a vital role as catalysts in the synthesis of bulk and fine chemicals, while their commercial use as catalysts for hydroformylation<sup>1</sup> and acetic acid formation through methanol carbonylation is well documented.<sup>2</sup> Much of the interest in using carbon monoxide as a ligand in transition-metal organometallic chemistry arises from the fact that it is an industrially available C<sub>1</sub> synthon that binds strongly to electron-rich, low oxidation state d-block metal complexes. The latter property is a primary consequence of the well-established  $\sigma$ -donor and  $\pi$ -acceptor interactions between metal- and CO-based orbitals. In an octahedral complex, the metal d-orbitals with  $T_{2g}$  symmetry become strongly bonding, ensuring that transition-metal carbonyl compounds have a strong ligand field. This contrasts with the general case whereby 3d-metal complexes show weaker metal–ligand interactions<sup>3</sup> and so exhibit smaller ligand fields than their 4d and 5d counterparts, making them more prone to one-electron oxidation reactions.<sup>4</sup> The tendency for CO ligands in 3d-metal complexes to enforce low-spin electronic configurations and reduce unwanted redox reactions<sup>5</sup> has thus led to significant

interest in their development as sustainable alternatives to the currently used 4d and 5d equivalents.<sup>4,6–8</sup>

A second important consequence of the  $\sigma$ -donor and  $\pi$ -acceptor interactions between metals and carbonyl ligands is that the extent of the (mainly)  $\pi$ -acceptor interaction modulates the M–C and C $\equiv$ O bond strengths, which can be interrogated through changes to the frequencies of the vibrational modes of the carbonyl ligands.<sup>9</sup> Coupled with the strong dipole moment of the C $\equiv$ O bond, this means that infrared (IR) spectroscopy is an ideal tool to investigate the structure and dynamics of transition-metal carbonyl compounds.

The combination of 3d-metal carbonyls and IR spectroscopic analysis, including ultrafast time-resolved methods, has been used successfully in the application of simple manganese

Received: May 14, 2024

Revised: June 17, 2024

Accepted: June 18, 2024

carbonyl compounds, such as  $[\text{MnBr}(\text{CO})_5]$  and  $[\text{Mn}_2(\text{CO})_{10}]$ , to C–H bond functionalization reactions that couple heterocyclic substrates with a range of different electrophiles (Figure 1a). Detailed mechanistic studies have shown that cyclo-

(a) Exemplar Mn-catalyzed C–H Bond Functionalisation Reaction



(b) Key steps observed by time-resolved infra-red spectroscopy, with timescales shown

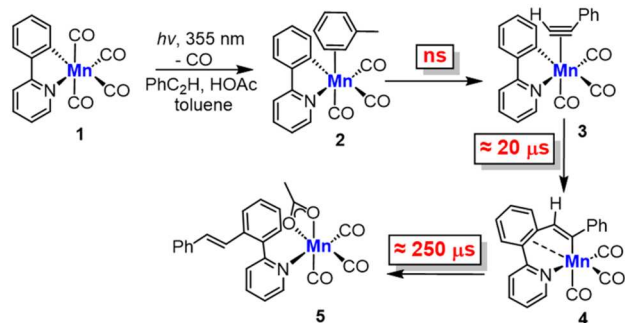


**Figure 1.** (a) Exemplar Mn-catalyzed C–H bond functionalization reaction<sup>10</sup> and (b) summary of results from previous time-resolved spectroscopic studies involving **1**.<sup>5</sup>

manganated compounds, such as  $[\text{Mn}(\text{ppy})(\text{CO})_4]$ ,<sup>7,10–12</sup> **1** (ppy = cyclometalated 2-phenylpyridine) are key intermediates and viable precatalysts in these reactions. The key catalytic steps mediated by **1** have been investigated by time-resolved ultraviolet (UV) pump–IR probe spectroscopy experiments spanning time scales from ps to ms (Figure 1b). In these experiments, the UV pump induces an ultrafast CO dissociation from **1**,<sup>13</sup> simulating the same process that happens under thermal catalytic conditions. This results in the formation of complexes *fac*- $[\text{Mn}(\text{ppy})(\text{CO})_3\text{S}]$  (S = solvent molecule) and insight into the nature of the photoproducts was obtained from the energy and symmetry of the strong vibrational modes of the three remaining CO ligands. By observing changes to the bands over time, details of the subsequent dynamics of the complex were obtained. In complex mixtures that simulate catalytic reactions, it was further demonstrated that the initial binding event is kinetically controlled<sup>14,15</sup> with Mn coordinating in the first place to the solvent (the most abundant species) to form **2** (in toluene solution) (Figure 1b). A ligand substitution by, for example, phenylacetylene then yielded **3**. Importantly, it was possible to directly observe the migratory insertion reaction of the alkyne into the Mn–C bond, a key step underpinning the catalytic reaction, to give **4**.<sup>16–19</sup> Performing the experiment in the presence of HOAc allowed for the observation of a slower protonolysis of the Mn–C bond to reveal **5**,<sup>20</sup> which has the product from the reaction bound to the metal. Therefore, this approach has enabled key catalytic steps mediated by the metal to be directly observed.<sup>5</sup>

The ability of IR spectral analysis of the photoproducts formed from **1** to give unique insights into the mechanistic behavior of the Mn precatalyst establishes a requirement to obtain a comprehensive understanding of the nature of the vibrational modes of this molecule. Such information will not only support the assignment of time-resolved spectra but also provide a means to interpret the fundamental nature of the

precatalyst and its interaction with the molecular environment to guide future modifications. Of particular importance is the question of the vibrational coupling of the CO-stretching modes ( $\nu_{\text{CO}}$ ) to one another and with the organic ligand, as changing the structure of this group profoundly influences reactivity.<sup>14,15,18</sup> A related issue is the mechanism of vibrational energy management by the complex, which will impact reaction dynamics.

In this manuscript, we report an investigation into the carbonyl ligand vibrational manifold of  $[\text{Mn}(\text{ppy})(\text{CO})_4]$  (Figure 1b, **1**) using ultrafast 2D-IR spectroscopy. 2D-IR has been widely applied to study metalcarbonyl species, providing insights into vibrational potential energy surfaces,<sup>21–23</sup> solvent–solute interactions,<sup>24–29</sup> equilibrium dynamics,<sup>30</sup> and real-time evolution of photoactivated molecules.<sup>24,31–34</sup> These have included several studies of catalytically relevant species<sup>26,31–33</sup> including bioinspired systems.<sup>35–38</sup> By comparing 2D-IR data with anharmonic density functional theory (DFT) calculations, we establish inter-mode couplings and solution phase structural parameters for the  $\nu_{\text{CO}}$  modes of **1** in addition to measuring the vibrational relaxation dynamics of **1** in a range of solvents relevant to catalytic functionality. We show that these data provide a detailed picture of the complex potential energy surfaces and bonding of **1**, establishing a fundamental basis for the next steps in understanding precatalyst behavior.

## EXPERIMENTAL SECTION

### Synthesis and Characterization of **1**

Compound **1** was synthesized and characterized following procedures reported elsewhere.<sup>39</sup> A detailed description is provided in the electronic Supporting Information (ESI).

### Sample Preparation for IR Spectroscopy

The samples for all IR spectroscopy experiments were prepared by dissolving 0.8 mg/mL **1** in dry deoxygenated *n*-heptane solvent (~2.5 mM). A 500  $\mu\text{L}$  aliquot of this solution was placed into a transmission cell (Harrick) featuring two  $\text{CaF}_2$  windows separated by a PTFE spacer (thickness: 200  $\mu\text{m}$ ) to specify the optical path length.

### IR Absorption Spectroscopy

IR absorption spectra were recorded in transmission mode at room temperature using a Bruker Vertex 80 FTIR spectrometer with a spectral resolution of 1  $\text{cm}^{-1}$ . The empty spectrometer under the  $\text{N}_2$  atmosphere was used to acquire background spectra for the measurements. All spectra reported were the average of 32 scans.

### 2D-IR Spectroscopy

The two-dimensional infrared (2D-IR) spectrometer consisted of two Yb-based amplified lasers (Pharos 20W and Pharos 10W, Light Conversion) synchronized by a single, common oscillator. The amplifiers were each used to pump an optical parametric amplifier (OPA, Orpheus Mid-IR, Light Conversion) equipped with difference frequency generation (Lyra, Light Conversion) to produce independently tunable sources for one- or two-color 2D-IR spectroscopy. In the mid-IR, the two OPAs produce usable bandwidths of  $>200 \text{ cm}^{-1}$  with energies of 2.5 and 1.5  $\mu\text{J}/\text{pulse}$ , respectively, at a pulse repetition rate of 50 kHz.

2D-IR data collection was achieved using a 2DQuick spectrometer (Phasetech). The spectrometer employs the pump–probe beam geometry for 2D-IR data collection<sup>40–42</sup> and uses a mid-IR pulse shaper to generate and control the time delay ( $\tau$ ) between the pair of “pump” pulses. The waiting time ( $T_w$ ) between the second pump and probe pulses was determined by an optical delay line. Signal measurement was achieved via twin 64-element HgCdTe array detectors configured to allow simultaneous collection of either signal and reference or ZZZZ (parallel) and ZZZY (perpendicular) polarization-resolved data.

In the experiments that follow, the output of OPA pumped by the Pharos 20W amplifier was used to create all three infrared pulses (two pumps, one probe). All pulses were centered at  $2000\text{ cm}^{-1}$ , resonant with the  $\nu_{\text{CO}}$  modes of **1**. For a given value of  $T_w$ ,  $\tau$  was scanned in steps of 20 fs to a maximum delay time of 4 ps applying a rotating frame frequency of  $1585\text{ cm}^{-1}$ . Each 2D-IR plot represents the average of 500 spectra, repeated 3 times, taking  $\sim 2$  min to acquire.

### Density Functional Theory Calculations

DFT calculations were performed with Gaussian 16, Revision C.02,<sup>43</sup> using the bp86 functional and def2-sv(p) basis set and an ultrafine integration grid. The heptane solvent was treated with an SCRf model. The geometry of **1** was optimized and confirmed as a minimum by an absence of negative frequency vibrational modes. Anharmonic vibrational frequency calculations were performed using the *freq = anarm* keyword.

## RESULTS

### Infrared Absorption Spectroscopy

The IR spectrum of **1** in heptane solution is shown in Figure 2. Four bands are visible in the region of  $1940\text{--}2080\text{ cm}^{-1}$ ,

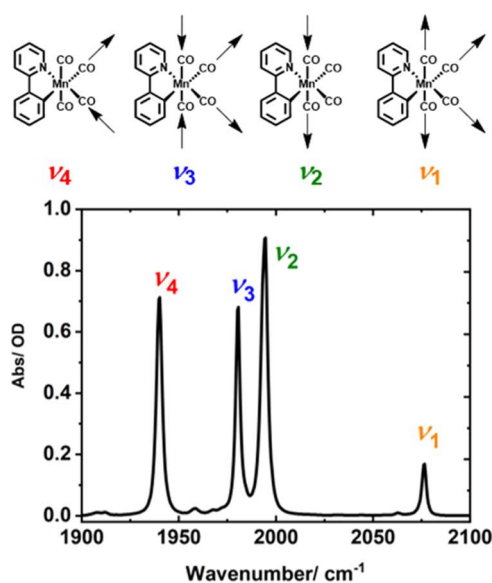


**Figure 2.** Top: Schematic diagram illustrating the vibrational modes of  $[\text{Mn}(\text{ppy})(\text{CO})_4]$  **1**. Bottom: FTIR spectrum of 0.8 mg/mL solution of **1** in *n*-heptane.

consistent with previous studies.<sup>13</sup> These bands have been assigned to the  $\nu_{\text{CO}}$  modes ( $\nu_{1-4}$ ) shown in Figure 2. Based on a  $C_s$  point group description of **1**, we identify these as  $3A'$  ( $\nu_{1,3,4}$ ) and  $1A''$  ( $\nu_2$ ) symmetry modes. To aid with a comparison with the related isoelectronic systems  $[\text{Cr}(\text{bpy})(\text{CO})_4]$ <sup>44</sup> and  $[\text{Re}(\text{bpy})(\text{CO})_4]$ <sup>45</sup> (bpy = 2,2'-bipyridyl), we note that if an approximation to the higher symmetry  $C_{2v}$  point group for **1** is assumed, then these can be assigned to  $2A_1$  ( $\nu_{1,3}$ ),  $B_1$  ( $\nu_2$ ), and  $B_2$  ( $\nu_4$ ). For clarity, in the discussion that follows, we will refer to the bands using the  $\nu_{1-4}$  terminology shown in Figure 2.

### 2D-IR Spectroscopy

The 2D-IR spectrum of **1** in heptane solution at a  $T_w$  value of 500 fs (Figure 3a) shows a number of peaks. On the diagonal of the spectrum (pump frequency = probe frequency, dashed black line), four blue (negative) peaks can be seen, which coincide with the four bands in the IR absorption spectrum of **1**, which is shown alongside the 2D-IR plot for comparison. These diagonal peaks can be assigned to the  $v = 0\text{--}1$  transitions of the  $\nu_{1-4}$

modes. Each blue diagonal peak is accompanied by a red (positive) peak shifted between 8 and  $12\text{ cm}^{-1}$  to lower probe frequency. These peaks are assigned to the corresponding  $v = 1\text{--}2$  transitions of the  $\nu_{1-4}$  modes. The frequency separation of the positive and negative ( $v = 1\text{--}2$  and  $v = 0\text{--}1$ ) peaks is due to the anharmonicity of the vibrational potentials. By fitting Gaussian lineshapes to horizontal slices through the spectrum in Figure 3a at pump frequencies corresponding to modes  $\nu_1$  to  $\nu_4$ , the values of the anharmonic shifts for each of the four modes were evaluated and these are listed in Table 1 (left side, gray boxes).

Also visible in Figure 3a are peaks in the off-diagonal part of the 2D-IR spectrum. At short values of  $T_w$  relative to the vibrational relaxation time of **1** (see below), as in Figure 3a ( $T_w = 500$  fs), these off-diagonal peaks indicate the presence of vibrational coupling between the  $\nu_{\text{CO}}$  modes. Using the gray dashed guidelines (Figure 3a) it is clear that each of the four diagonal peaks is linked to the remaining three modes by such off-diagonal features, which each appear as a pair of negative and positive peaks. These peak pairs are most clearly visible in the top left and bottom right corners of the spectrum in Figure 3a, identified with arrows in Figure 3a. The off-diagonal peaks marked with arrows can be assigned to the coupling of modes  $\nu_1$  to  $\nu_4$  ( $\nu_1\nu_4$ ; top left, where the first term of  $\nu_1\nu_4$  indicates the pumped mode) and the reverse process ( $\nu_4\nu_1$ ; bottom right), respectively. The spectroscopic origin of the off-diagonal peak pair can be understood using the  $\nu_1\nu_4$  off-diagonal feature as an example. The pumped mode is  $\nu_1$  and the presence of negative and positive components in the off-diagonal feature arises from transitions due to the  $v = 0\text{--}1$  transition of the coupled mode ( $\nu_4$ , negative) and a transition (positive peak) from  $v = 1$  of the pumped mode ( $\nu_1$ ) to the combination band featuring one quantum of excitation in both of the modes (one each in  $\nu_1$  and  $\nu_4$ ). The vibrational coupling of modes  $\nu_1$  and  $\nu_4$  causes the energy of the combination state to be shifted in energy from the sum of the two fundamental transitions by the off-diagonal anharmonicity, which is a direct measure of the coupling strength of the two modes. This means that, for any pair of coupled modes, we can obtain a measure of the coupling strength from the separation of the negative and positive components of the off-diagonal peak linking the respective diagonal peaks.<sup>42</sup>

Once again, fitting Gaussian lineshapes to horizontal slices through the spectrum allows these off-diagonal anharmonic shifts, or coupling strengths, to be evaluated for each pair of  $\nu_{\text{CO}}$  modes of **1** (Table 1, colored cells). The values vary quite markedly from the very strong ( $\nu_1\nu_2$  and  $\nu_3\nu_4$ :  $18\text{--}20\text{ cm}^{-1}$ ), exemplified in Figure 3b, to comparatively weak ( $\nu_1\nu_4$ ,  $\nu_2\nu_3$ , and  $\nu_3\nu_1$ :  $5\text{--}8\text{ cm}^{-1}$ , Figure 3c). One particularly interesting example shows the presence of negative coupling between modes  $\nu_2$  and  $\nu_4$  ( $\nu_2\nu_4 = -2\text{ cm}^{-1}$ ), for which the probe frequency ordering of the negative and positive components of the off-diagonal peak pair is reversed relative to all of the others (Figure 3d).

In addition to obtaining coupling parameters between the pairs of  $\nu_{\text{CO}}$  modes, the off-diagonal peaks in a 2D-IR spectrum can be used to extract information relating to the angles between transition dipole moment (TDM) directions for each pair of modes.<sup>22,42</sup> This is achieved by comparing the relative amplitudes of diagonal and off-diagonal peaks linking a given pair of coupled vibrational modes in 2D-IR spectra obtained using parallel (ZZZZ) and perpendicular (ZZYY) pulse polarization geometries.<sup>22,42</sup> Performing this analysis for off-diagonal peaks that are relatively free of strong overlaps with other peaks allowed extraction of angles of  $90^\circ$ , within

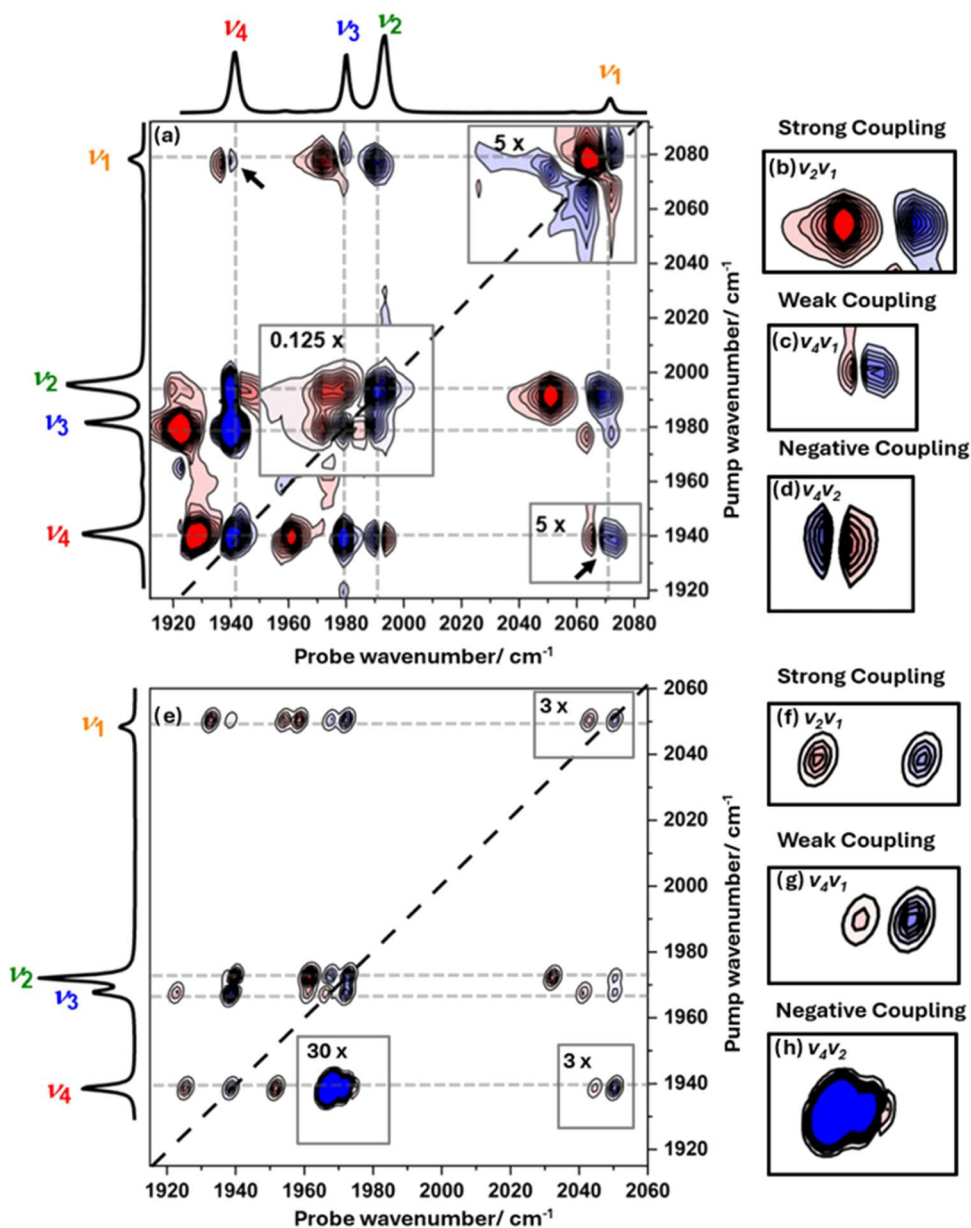


**Figure 3.** (a) 2D-IR spectrum of **1** in *n*-heptane solution measured at  $T_w = 500$  fs using ZZZY polarization alongside IR absorption spectra for comparison. Regions of the 2D-IR spectrum have been scaled for clarity and these are indicated by gray boxes with the magnification factor shown. (b–d) Enlarged sections of the spectrum in (a) focusing on off-diagonal peaks, which exemplify (b) strong coupling between modes  $\nu_2$  and  $\nu_1$ , (c) weak coupling between modes  $\nu_4$  and  $\nu_1$ , and (d) negative coupling between modes  $\nu_4$  and  $\nu_2$  as discussed in the text. Panel (e) shows a simulated 2D-IR spectrum based on the results of anharmonic DFT calculations for comparison (see the text and SI). (f–h) The same expanded regions in the predicted spectrum as in (b–d). The color scale for all plots runs from blue (negative) to red (positive).

experimental error, for  $\nu_1\nu_2$ ,  $\nu_1\nu_4$ ,  $\nu_2\nu_4$ , and  $\nu_3\nu_4$  (red figures in Table 1 and Figure S1).

#### DFT Calculations

Anharmonic DFT calculations were used to predict the vibrational frequencies and intensities of the fundamental  $\nu_{\text{CO}}$  transitions of **1** as well as the frequencies of transitions from the  $v = 1$  levels of each mode to higher-lying vibrational states. As this enables predictions of the  $v = 1-2$  transition frequencies for each of the  $\nu_{\text{CO}}$  modes and the frequencies of transitions to combination states, direct comparisons of the results of the calculation with all of the transition frequencies extracted from the 2D-IR spectroscopy data are possible. The numerical results of the simulations are shown in Table S1, but for ease of comparison with the 2D-IR data, we have used the values to

produce a simulated 2D-IR spectrum (Figure 3e) in which peak positions produced from the DFT-predicted transitions are represented by a 2D-Gaussian lineshape function (see the SI). The result of this process shows that the agreement between experiment and theory is excellent. Although the precise predictions of the (unscaled) frequencies of the fundamental bands are slightly different from the measured values, as would be anticipated, the mode separations are well reproduced along with the relative intensities of the bands in the IR absorption spectrum. Of particular relevance to our 2D-IR study, there is very close agreement between the coupling parameters obtained from experiment and calculation. This is manifest in the accurate reproduction of the experimental off-diagonal peak patterns (Figure 3a) in the simulated spectrum (Figure 3e) including

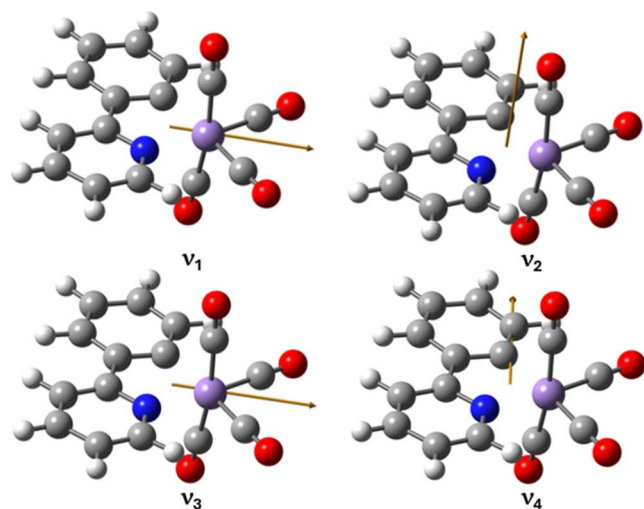
**Table 1. Left: Diagonal and Off-diagonal Anharmonicities Derived from Figure 3a (cm<sup>-1</sup>)<sup>a</sup>**

	Anharmonic shift / cm <sup>-1</sup>				Angle between TDM / °			
	$\nu_4$	$\nu_3$	$\nu_2$	$\nu_1$	$\nu_4$	$\nu_3$	$\nu_2$	$\nu_1$
$\nu_1$	5	-	18	7	90	180	90	-
$\nu_2$	-2	7	12	18	90	90	-	90
$\nu_3$	20	8	6	8	90	-	90	180
$\nu_4$	14	19	-3	7	-	90	90	90

<sup>a</sup>Gray cells represent the diagonal anharmonicities, and colored cells highlight off-diagonal anharmonicities between common pairs of modes. The pumped mode is indicated in the left-hand column so that the layout of the table resembles the 2D-IR spectrum. Right: Angles (°) between transition dipole moments (TDM) of modes  $\nu_{1-4}$  determined from 2D-IR data by off-diagonal peak anisotropy values (see the text). Figures in red show experimentally determined values while those in black are predicted via DFT calculations. Note the agreement between measured and predicted values for the same pairs of modes appearing on the opposite sides of the diagonal, which is indicated by gray boxes.

those with strong, weak, and negative couplings measured for **1**, highlighted above (see Figure 3f–h).

The outputs of the DFT calculations were also used to predict the vectors of TDMs for each of the  $\nu_{CO}$  modes (Figure 4), and

**Figure 4.** Figure showing the vectors of the transition dipole moments associated with each of the  $\nu_{CO}$  modes of **1**.

the angles between them agree very well with those calculated from the polarization-resolved 2D-IR spectra (*cf* red and black values in Table 1). This not only provides confidence in the band assignments of the modes in the spectrum but also confirms the solution phase structure of the precatalyst for the first time.

### Vibrational Dynamics

Alongside the IR spectroscopy and solution phase structure of **1** in the electronic ground state, 2D-IR, in combination with IR pump–probe spectroscopy, was used to interrogate the vibrational energy relaxation mechanisms and rotational dynamics of **1** in solution. The effect of vibrational relaxation on the 2D-IR spectrum of **1** is shown in Figure 5 (and over a larger range of time scales in Figure S2) in which the spectrum at a short value of  $T_w$  (500 fs) is compared with one obtained at  $T_w = 20$  ps. Three main changes to the spectrum occur during the

increased  $T_w$  period: (1) All of the peaks in the spectrum diminish in absolute intensity; (2) off-diagonal peaks observed in the short  $T_w$  spectrum are still present, but somewhat larger relative to the diagonal peak with the same pump frequency; and (3) a set of new peaks appear in the spectrum, and these are highlighted by green boxes in Figure 5b and labeled (a–m).

**Vibrational Relaxation.** The overall reduction in peak amplitudes across the spectrum as  $T_w$  increases occurs as a result of vibrational relaxation. The pump process in a 2D-IR experiment leads to a population of the  $\nu = 1$  levels of modes  $\nu_1$ – $\nu_4$ . These populations relax to the respective ground vibrational states with dynamics governed by the vibrational lifetime ( $T_1$ ) of the  $\nu = 1$  level of each of the modes. For simplicity, the  $T_1$  time scales for each of the modes of **1** were determined using IR pump–probe spectroscopy, and results from a number of solvents were compared. The recovered vibrational relaxation time for each  $\nu_{CO}$  mode (Figure S3) is shown in Table 2. It is noticeable from these results that, despite the solvents ranging from nonpolar heptane and toluene to polar THF and acetonitrile, the vibrational relaxation time does not show the kind of large variations that are often observed for metalcarboxyls in solution,<sup>28,34,46</sup> with the values in all four solvents falling in the range of 30–50 ps. Indeed, the values of 44–59 ps for modes  $\nu_1$ – $\nu_4$  determined for **1** in heptane are considerably faster than might be expected based on previous studies of alkane-solvated metalcarboxyls.<sup>46–48</sup>

**Intramolecular Vibrational Redistribution.** The growth of off-diagonal peak amplitudes relative to the diagonal peaks and the appearance of new peaks in the 2D-IR spectrum as  $T_w$  increases have been observed in similar systems previously<sup>22</sup> and can both be assigned to the process of intramolecular vibrational redistribution (IVR). In this process, the pump pulse excites a given mode ( $\nu_1$ – $\nu_4$ ) of **1**, populating the  $\nu = 1$  level, but the fast transfer of this population between all of the  $\nu_{CO}$   $\nu = 1$  levels occurs so that, on the IVR time scale, an equilibrium is established between the  $\nu = 1$  populations. This population then relaxes with the  $T_1$  times of the individual modes.

While IVR is often manifest in the dynamics of diagonal and off-diagonal peaks via the appearance of biexponential behavior, the clearest indication of IVR in the 2D-IR spectrum of **1** can be seen via the appearance of new peaks in the spectrum as  $T_w$  increases (Figure 5b). These are observed because population transfer from the  $\nu = 1$  level of the pumped mode to the  $\nu = 1$  level of a nonpumped mode allows observation of the  $\nu = 1$ – $2$  transition of the newly populated mode, which is not present at shorter values of  $T_w$ . This leads to new, positive off-diagonal peaks appearing at the  $\nu = 1$ – $2$  frequency of the nonpumped mode. In a system such as **1**, where strong mode couplings mean that the positions of the positive components of the off-diagonal peaks caused by coupling (visible at short  $T_w$ , Figure 5a) are separated from the positions of the  $\nu = 1$ – $2$  transitions of the modes populated by IVR by more than the spectral line width, new peaks appear. This is further exemplified in Figure 5c–f and highlighted by the cyan boxes and labeled (a–m).

Measuring 2D-IR spectra as a function of  $T_w$  (Figure S2) and fitting the growth time scales of the new bands due to IVR (a–m) to exponential functions (Figure S4) enabled quantification of the IVR time scales for each of the new peaks (Table 3). While mode dependent, IVR generally occurs on sub-10 ps time scales for **1** in heptane, though the two examples where the pumped and IVR-populated mode show the greatest frequency separation (peaks a and m), involving energy transfer between modes  $\nu_1$  and  $\nu_4$ , show the longest time scales (~13–20 ps).

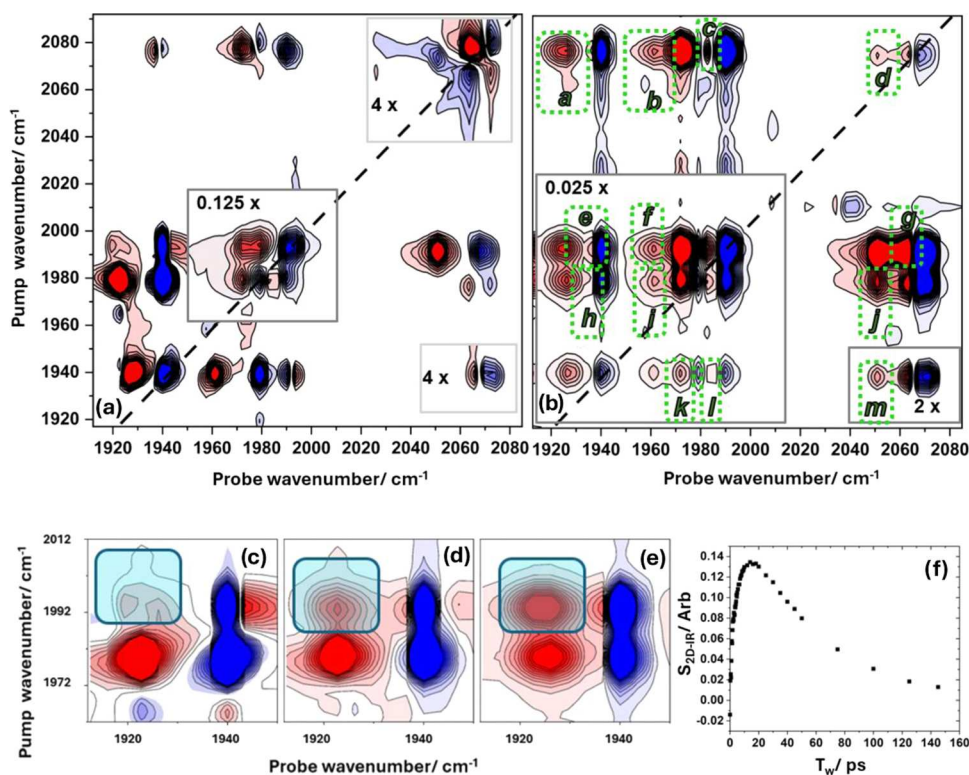


**Figure 5.** (a) 2D-IR spectrum of **1** in *n*-heptane solution measured at  $T_w$  of 500 fs (ZZYY). (b) 2D-IR spectrum of **1** in *n*-heptane solution measured at  $T_w$  of 20 ps (ZZYY). New peaks appearing due to energy transfer (IVR) are highlighted using green boxes and labeled (a–m). The spectrum in (b) has been scaled by a factor of 40 to make smaller peaks visible. Panels (c–f): Expanded regions of 2D-IR spectra of **1** at a number of values of  $T_w$ , showing the temporal evolution of peak e from (b).  $T_w$  values are (c) 250 fs, (d) 2.0 ps, and (e) 14 ps. The off-diagonal peak e, highlighted by the box, increases in intensity due to IVR. The full temporal evolution of the peak is shown in (f), where the amplitude decay is due to vibrational relaxation. In each of the 2D-IR plots, the color scale runs from red (positive) to blue (negative). The scale is common to all plots.

**Table 2. Vibrational Lifetimes ( $\nu_1$ – $\nu_4$ , ps) and Anisotropy Parameters ( $\nu_2$ , ps) Determined by IR Pump–Probe Spectroscopy for **1** in Solvents of Different Properties<sup>a</sup>**

solvent	vibrational relaxation, $\tau$ /ps				anisotropy $\nu_2$ $\tau$ /ps
	$\nu_1$	$\nu_2$	$\nu_3$	$\nu_4$	
<i>n</i> -heptane	59 ± 5	48 ± 1	44 ± 2	49 ± 1	13 ± 3
toluene	38 ± 1	36 ± 1		38 ± 1	7 ± 1
THF	37 ± 2	31 ± 2		36 ± 1	8 ± 2
CH <sub>3</sub> CN	44 ± 1	40 ± 2		42 ± 1	4 ± 1

<sup>a</sup>The experimental data were best represented by a biexponential decay function including a fast component of  $\sim 1$  ps for both the vibrational relaxation and the anisotropy, which is assigned to an instrument response.

This is as expected because conservation of energy requires the mismatch in energies between the pumped and IVR-populated modes to be made up via the low-frequency modes of the solvent acting as a thermal bath for receiving or donating energy.<sup>49–51</sup> The latter modes are populated according to the Boltzmann distribution and represent a reservoir of up to  $\sim 200$  cm<sup>-1</sup> at room temperature. In the case of modes  $\nu_1$  and  $\nu_4$ , which are separated by 140 cm<sup>-1</sup>, IVR is occurring through the tail of this thermal distribution leading to a reduced rate.<sup>52</sup> It is noticeable that the downhill energy transfer rate, where the pumped mode lies higher in energy than the receiving mode (peak a;  $\nu_1 - \nu_4$ ,  $\tau = 13$  ps), is faster than the uphill process (peak m,  $\nu_4 - \nu_1$ ,  $\tau = 22$  ps), consistent with the principle of detailed balance.

**Anisotropy.** The results of IR pump–probe spectroscopy measurements obtained as a function of input pulse polarization

**Table 3. IVR Time Scales (ps) for the Growth of Energy Transfer Peaks a–m<sup>a</sup>**

IVR peak	$\tau$ ps	approx mode separation cm <sup>-1</sup>
a	13 ± 2	140
b		100
c	5 ± 1	85
d	2 ± 1	
e	2 ± 1	55
f	4 ± 1	15
g	3 ± 1	85
h	8 ± 2	40
i		
j	5 ± 1	100
k	6 ± 1	40
l	11 ± 2	55
m	22 ± 3	140

<sup>a</sup>The nomenclature refers to the assignments given in Figure 5b. Mode separations are identified using pairs of diagonal modes ( $\nu_{1-4}$ ) that link the new off-diagonal features appearing due to IVR.

were used to investigate the rotational dynamics of **1** in solution via the anisotropy parameter (Figure S5 and Table 2). Focusing on the  $\nu_2$  mode of **1**, which yielded the strongest signals, the anisotropy was found to be well represented by a double exponential function in all solvents. The shorter component was found to be less than 1 ps and is assigned to an instrument response. The longer component in heptane was 13 ps, which we assign to rotational relaxation of **1**. This is consistent with rotational time scales observed for metalcarbonyls of similar

size in alkane solutions.<sup>26,38</sup> In more polar solvents, the observed time scale reduced to 4–8 ps. However, the separation between this value and the measured IVR time scale for **1** makes it difficult to assign the time scale definitively to molecular rotation because IVR between  $\nu_{\text{CO}}$  modes will lead to a scrambling of the dipole moment direction of the molecules, similar to the effect of molecular reorientation.

**Coherent Dynamics.** Examination of the 2D-IR spectra of **1** in heptane also showed that the intensities of both diagonal and off-diagonal peaks were observed to oscillate with  $T_w$  (Figure S6). These effects arise as a result of coherent processes involving simultaneous excitation of more than one  $\nu_{\text{CO}}$  mode of **1** and have been observed previously.<sup>21</sup> In the case of off-diagonal peaks, these are observed to oscillate at a frequency that matches the frequency separation of the involved, coupled, modes while diagonal peaks oscillate at frequencies that match the separations between the excited modes and other close-lying diagonal modes. Examples are shown in Figure S6 involving the diagonal peak corresponding to mode  $\nu_1$  and the off-diagonal peak linking mode  $\nu_1$  with  $\nu_2$  ( $\nu_2\nu_1$ ). Both were observed to oscillate at a frequency equivalent to  $75 \pm 1 \text{ cm}^{-1}$ , which corresponds to the frequency spacing of modes  $\nu_1$  and  $\nu_2$  (Figure 2). The dephasing time of the oscillations (2.5 ps) gives further insight into the time scale of local fluctuations of the molecule and solvent, which leads to loss of the coherence with time. In previous studies, it has been established that diagonal peak oscillations occur via the nonrephasing pathways that contribute to the 2D-IR signal while the off-diagonal peak oscillations occur via the rephasing pathways.<sup>21</sup> These are observed simultaneously in our data because the pump–probe geometry collects both rephasing and nonrephasing terms.

## DISCUSSION

One of the main benefits of applying 2D-IR spectroscopy to metalcarbonyl systems is the ability to gain detailed insight into the specific nature of the vibrational modes and potential energy surfaces of a molecule. In the case of **1**, the data show that the  $\nu_{\text{CO}}$  modes are all mutually coupled. The implication is that excitation of any of the modes influences the frequencies of the remaining three such that the modes are delocalized to some degree across the four carbonyl ligands. This is also shown by the results of anharmonic DFT calculations.

The extent of the coupling and so delocalization does however vary between the modes. Although one of the primary factors in governing mode coupling strength is often the frequency separation of the modes, this does not account for the trend observed here. Alternatively, the observations may be rationalized by considering the nature of the atomic displacements involved in each mode (Figure 1). The most obvious case involves the pair of modes  $\nu_2$  and  $\nu_4$ , which exhibit a negative coupling. Examination of the atomic displacements shows that these two modes that are almost entirely located on either the axial ( $\nu_2$ ) or the equatorial ( $\nu_4$ ) ligands, suggesting that this minimizes the coupling interaction. Considering the mode pairs that show positive couplings, very strong coupling occurs between modes  $\nu_1$  and  $\nu_2$  and between  $\nu_3$  and  $\nu_4$  ( $17 \text{ cm}^{-1}$ ). Conversely, the coupling between modes in these two groups (i.e.,  $\nu_1-\nu_4$ ;  $\nu_1-\nu_3$ ;  $\nu_2-\nu_3$ ) is weaker, though not insignificant ( $5-8 \text{ cm}^{-1}$ ). The origins of these effects are less clear. While the DFT results indicate that there is a slightly greater involvement of the axial ligand pair in mode  $\nu_1$  and the equatorial ligand pair in mode  $\nu_3$ , there is sufficient delocalization to preclude assignment to solely axial or equatorial ligand modes and so

no simple attribution can be made. This may also represent the fact that in  $C_{2v}$  complexes  $[\text{M}(\text{L-L})(\text{CO})_4]$ , the  $d_\pi$  orbitals split so that the orbital in the same plane as the L-L ligand (normally denoted as  $d_{x^2-y^2}$ )<sup>53,54</sup> makes a contribution to HOMO. The other two  $d_\pi$  orbitals ( $d_{xz}$  and  $d_{yz}$ ) make contributions to HOMO–1 and HOMO–2, which are similar energies.<sup>45,53</sup> The latter two orbitals are, therefore, distinct from  $d_{x^2-y^2}$  and are involved in  $\pi$ -back bonding to the two mutually *trans* CO ligands.

When considering the vibrational dynamics of **1** in solution, it is noticeable that rapid energy transfer between the  $\nu_{\text{CO}}$  modes is a key feature of the vibrational energy relaxation mechanism. This process has been widely observed in  $\text{M}(\text{CO})$  species.<sup>28,29</sup> The time scales for IVR between all modes is on the order of 5–10 ps, except for transfer between modes that show the greatest energy separation as described above. These observations are comparable with those on similar molecules in heptane solution.<sup>28,34,55</sup> It is noticeable that the strength of the mode couplings discussed above does not clearly correlate with IVR time scales, though extraction of rates for a single mode-to-mode transfer is challenging in such a complicated system with overlapping peaks and multidirectional energy transfer processes to consider. The IVR process is widely accepted to be solvent mediated, with the low-frequency modes of the solvent acting as a bath, accepting or donating excess energy during the IVR transitions.<sup>50</sup> This situation would dictate that the fastest energy transfer time would occur between modes that are separated by a frequency at which the low-frequency density of states of the solvent is at its peak.<sup>52</sup> Typically, this peak falls between 50 and 90  $\text{cm}^{-1}$  and pairs of modes with separations in this range do broadly show the faster IVR rates (Table 3), but this is by no means conclusive, perhaps again in part due to the complexity of the coupled manifold of  $\nu_{\text{CO}}$  states involved in this system.

In the case of the overall vibrational relaxation time, the values of around 50 ps derived for the four carbonyl stretching modes of **1** in heptane are very short in comparison to measurements on similar systems, where values closer to 100 ps have been measured.<sup>28,55</sup> One possibility is that the interactions between heptane and the  $\nu_{\text{CO}}$  modes of **1** are stronger than usual. However, there is no evidence for this from the IVR time scales. The measured IVR times in the 5 ps range are consistent with the previous work,<sup>55</sup> whereas strong solvent interactions would have been expected to lead to faster transfer rates. An alternative scenario is that the vibrational modes of **1** relax primarily via an intramolecular route. In particular, the large organic ligand of **1** will possess a significant number of low-frequency modes that might contribute to an increased number of channels for vibrational relaxation. This could explain the faster-than-usual relaxation times and the relative insensitivity of the relaxation time scale to the nature of the solvent, with values in the 30–50 ps range being measured across the four solvents studied. A related observation is that the lineshapes of the 2D-IR spectra showed little evidence of inhomogeneous broadening. This is consistent with previous studies carried out on metalcarbonyls in heptane solution<sup>28,55</sup> and reinforces the view of a relatively limited degree of solvent–solute interactions taking place. In light of this, it is interesting to note that in activated complexes  $[\text{Mn}(\text{N}^{\text{C}})(\text{solvent})(\text{CO})_3]$  where a solvent molecule replaces a photodissociated carbonyl ligand, the observed vibrational relaxation times are rather shorter. For example, in the imine analogues,  $T_1$  is  $26.4 \pm 0.8 \text{ ps}$ .<sup>15</sup> This is consistent with the binding of the solvent molecule increasing the solute–solvent

interactions and bypassing the intramolecular relaxation mechanism, though changing the organic ligand will also affect the precise nature and quantity of low-frequency modes available to participate in relaxation.

The aim of the current study was to gain more detailed insight into the fundamental nature of the precatalyst **1** as a means to provide a basis from which the catalytic mechanism can be understood and so offer a potential route to optimizing the performance of derivatives. In this endeavor, the results provide the first data point rather than a conclusive answer. However, it has been demonstrated that changing the cyclomanganated ligand has an impact on reactivity<sup>14,15,18</sup> and so this study establishes a baseline from which changes in molecular orbitals and bonding can be evaluated when different organic ligands are present. In addition, a first study of the interaction of the precatalyst with the solvent has been established, for comparison with later work. A more detailed investigation is now needed to establish whether these parameters link to reactivity, and if so, how. One potentially interesting avenue of enquiry would target coupling and energy transfer processes between CO and modes of the ppy ligand, though this lies beyond the scope of the current study.

It is especially encouraging to report the excellent agreement between DFT calculations and 2D-IR spectroscopy measurements in terms of predicting the mode descriptions, molecular structure, and couplings. As the latter arise from the complex interplay of the different normal mode potentials, this suggests that the predictive power of anharmonic DFT calculations will be a valuable tool in later studies, especially as a method to deconvolute the structure of reactive intermediates in catalytic cycles.

## CONCLUSIONS

In an effort to begin the process of understanding how the ground state potential energy surfaces and vibrational dynamics of a precatalyst species might influence reactivity, we have used 2D-IR spectroscopy in combination with anharmonic DFT calculations to study the molecule  $[\text{Mn}(\text{ppy})(\text{CO})_4]$  in solution. Measurements of the coupling constants and angular relationships between the transition dipole moments of the  $\nu_{\text{CO}}$  modes of **1** revealed the structure of **1** in solution. Determination of vibrational coupling parameters showed that all carbonyl stretching modes were coupled, indicating delocalization of the modes, though the absolute coupling strengths varied significantly depending on the precise nature of the atomic displacements, and so molecular orbitals, involved in each case. An investigation into the vibrational relaxation mechanism of **1** showed rapid IVR between the carbonyl stretching modes. A relative solvent independence of the overall vibrational relaxation time of **1** across a number of solvents of differing properties is suggestive of limited solvent–solute interactions.

Our study shows that the 2D-IR spectra of **1** show a rich and detailed pattern of off-diagonal peaks that are extremely well resolved such that we were able to clearly separate and identify contributions due to coupling and IVR. Such a nuanced spectral fingerprint would be useful in facilitating the evaluation of mixtures of species, for example, at points along the reaction coordinate as the nature of the catalytic species present altered. The ability to measure 2D-IR spectra on short time scales also opens up the interesting possibility of performing such analyses in real time. Of particular interest in subsequent studies will be how strongly the nature of the organic bidentate ligand

modulates the measured parameters, given the clear role that this moiety plays in modulating reactivity.

## ASSOCIATED CONTENT

### Supporting Information

The Supporting Information is available free of charge at <https://pubs.acs.org/doi/10.1021/acsphyschemau.4c00037>.

Details of synthesis methods, additional ultrafast spectroscopy data, and analysis and results of DFT calculations (PDF)

## AUTHOR INFORMATION

### Corresponding Authors

**Jason M. Lynam** – Department of Chemistry, University of York, York YO10 5DD, U.K.; [orcid.org/0000-0003-0103-9479](https://orcid.org/0000-0003-0103-9479); Email: [jason.lynam@york.ac.uk](mailto:jason.lynam@york.ac.uk)

**Neil T. Hunt** – Department of Chemistry and York Biomedical Research Institute, University of York, York YO10 5DD, U.K.; [orcid.org/0000-0001-7400-5152](https://orcid.org/0000-0001-7400-5152); Email: [neil.hunt@york.ac.uk](mailto:neil.hunt@york.ac.uk)

### Authors

**Jonathan B. Eastwood** – Department of Chemistry, University of York, York YO10 5DD, U.K.

**Barbara Procacci** – Department of Chemistry and York Biomedical Research Institute, University of York, York YO10 5DD, U.K.; [orcid.org/0000-0001-7044-0560](https://orcid.org/0000-0001-7044-0560)

**Sabina Gurung** – Department of Chemistry and York Biomedical Research Institute, University of York, York YO10 5DD, U.K.

Complete contact information is available at:

<https://pubs.acs.org/10.1021/acsphyschemau.4c00037>

### Author Contributions

CRediT: **Jonathan Eastwood** data curation, formal analysis, investigation, validation, visualization, writing-original draft, writing-review & editing; **Barbara Procacci** data curation, formal analysis, investigation, validation, visualization, writing-original draft, writing-review & editing; **Sabina Gurung** data curation, investigation, resources, visualization, writing-review & editing; **Jason M. Lynam** conceptualization, funding acquisition, methodology, project administration, supervision, writing-original draft, writing-review & editing; **Neil T. Hunt** conceptualization, funding acquisition, methodology, project administration, supervision, writing-original draft, writing-review & editing.

### Notes

The authors declare no competing financial interest.

## ACKNOWLEDGMENTS

J.B.E., J.M.L., and N.T.H. would like to acknowledge the funding from EPSRC (EP/W031914/1). N.T.H. and S.G. also acknowledge the support from EPSRC (EP/W021404/1) while B.P. acknowledges the funding from the Leverhulme Trust (RPG-2021-160). J.M.L. is supported by a Royal Society Industry Fellowship (INF\R1\221057). The computational work in this project was undertaken on the Viking Cluster, a high-performance computing facility provided by the University of York. We are grateful for computational support from the University of York High Performance Computing service,

Viking and the Research Computing team. We are also grateful to Professor Ian Fairlamb (York) for insightful discussions and support for synthetic chemistry.

## REFERENCES

- (1) Hood, D. M.; Johnson, R. A.; Carpenter, A. E.; Younker, J. M.; Vinyard, D. J.; Stanley, G. G. Highly active cationic cobalt(II) hydroformylation catalysts. *Science* **2020**, *367*, 542–548.
- (2) Haynes, A.; Maitlis, P. M.; Morris, G. E.; Sunley, G. J.; Adams, H.; Badger, P. W.; Bowers, C. M.; Cook, D. B.; Elliott, P. I.; Ghaffar, T.; Green, H.; Griffin, T. R.; Payne, M.; Pearson, J. M.; Taylor, M. J.; Vickers, P. W.; Watt, R. J. Promotion of iridium-catalyzed methanol carbonylation: mechanistic studies of the cativa process. *J. Am. Chem. Soc.* **2004**, *126*, 2847–2861.
- (3) Kaupp, M. The role of radial nodes of atomic orbitals for chemical bonding and the periodic table. *J. Comput. Chem.* **2007**, *28*, 320–325.
- (4) Zell, T.; Langer, R. From Ruthenium to Iron and Manganese: A Mechanistic View on Challenges and Design Principles of Base-Metal Hydrogenation Catalysts. *ChemCatChem* **2018**, *10*, 1930–1940.
- (5) Fairlamb, I. J. S.; Lynam, J. M. Unveiling Mechanistic Complexity in Manganese-Catalyzed C-H Bond Functionalization Using IR Spectroscopy Over 16 Orders of Magnitude in Time. *Acc. Chem. Res.* **2024**, *57*, 919–932.
- (6) Liu, W.; Ackermann, L. Manganese-Catalyzed C–H Activation. *ACS Catal.* **2016**, *6*, 3743–3752.
- (7) Hu, Y.; Zhou, B.; Wang, C. Inert C-H Bond Transformations Enabled by Organometallic Manganese Catalysis. *Acc. Chem. Res.* **2018**, *51*, 816–827.
- (8) Papa, V.; Cao, Y. X.; Spannenberg, A.; Junge, K.; Beller, M. Development of a practical non-noble metal catalyst for hydrogenation of N-heteroarenes. *Nat. Catal.* **2020**, *3*, 135–142.
- (9) Turner, J. J.; George, M. W.; Poliakov, M.; Perutz, R. N. Photochemistry of transition metal carbonyls. *Chem. Soc. Rev.* **2022**, *51*, 5300–5329.
- (10) Zhou, B.; Chen, H.; Wang, C. Mn-catalyzed aromatic C-H alkenylation with terminal alkynes. *J. Am. Chem. Soc.* **2013**, *135*, 1264–1267.
- (11) Hammarback, L. A.; Robinson, A.; Lynam, J. M.; Fairlamb, I. J. S. Delineating the critical role of acid additives in Mn-catalyzed C-H bond functionalisation processes. *Chem. Commun.* **2019**, *55*, 3211–3214.
- (12) Hammarback, L. A.; Robinson, A.; Lynam, J. M.; Fairlamb, I. J. S. Mechanistic Insight into Catalytic Redox-Neutral C-H Bond Activation Involving Manganese(I) Carbonyls: Catalyst Activation, Turnover, and Deactivation Pathways Reveal an Intricate Network of Steps. *J. Am. Chem. Soc.* **2019**, *141*, 2316–2328.
- (13) Aucott, B. J.; Duhme-Klair, A. K.; Moulton, B. E.; Clark, I. P.; Sazanovich, I. V.; Towrie, M.; Hammarback, L. A.; Fairlamb, I. J. S.; Lynam, J. M. Manganese Carbonyl Compounds Reveal Ultrafast Metal-Solvent Interactions. *Organometallics* **2019**, *38*, 2391–2401.
- (14) Eastwood, J. B.; Hammarback, L. A.; Burden, T. J.; Clark, I. P.; Towrie, M.; Robinson, A.; Fairlamb, I. J. S.; Lynam, J. M. Understanding Precatalyst Activation and Speciation in Manganese-Catalyzed C-H Bond Functionalization Reactions. *Organometallics* **2023**, *42*, 1766–1773.
- (15) Eastwood, J. B.; Hammarback, L. A.; McRobbie, M. T.; Clark, I. P.; Towrie, M.; Fairlamb, I. J. S.; Lynam, J. M. Time-resolved infra-red spectroscopy reveals competitive water and dinitrogen coordination to a manganese(I) carbonyl complex. *Dalton Trans.* **2020**, *49*, 5463–5470.
- (16) Hammarback, L. A.; Clark, I. P.; Sazanovich, I. V.; Towrie, M.; Robinson, A.; Clarke, F.; Meyer, S.; Fairlamb, I. J. S.; Lynam, J. M. Mapping out the key carbon-carbon bond-forming steps in Mn-catalyzed C-H functionalization. *Nat. Catal.* **2018**, *1*, 830–840.
- (17) Hammarback, L. A.; Bishop, A. L.; Jordan, C.; Athavan, G.; Eastwood, J. B.; Burden, T. J.; Bray, J. T. W.; Clarke, F.; Robinson, A.; Krieger, J. P.; Whitwood, A.; Clark, I. P.; Towrie, M.; Lynam, J. M.; Fairlamb, I. J. S. Manganese-Mediated C-H Bond Activation of Fluorinated Aromatics and the ortho-Fluorine Effect: Kinetic Analysis by Infrared Spectroscopic Analysis and Time-Resolved Methods. *ACS Catal.* **2022**, *12*, 1532–1544.
- (18) Hammarback, L. A.; Eastwood, J. B.; Burden, T. J.; Pearce, C. J.; Clark, I. P.; Towrie, M.; Robinson, A.; Fairlamb, I. J. S.; Lynam, J. M. A comprehensive understanding of carbon-carbon bond formation by alkyne migratory insertion into manganese cycles. *Chem. Sci.* **2022**, *13*, 9902–9913.
- (19) Burden, T. J.; Fernandez, K. P. R.; Kagoro, M.; Eastwood, J. B.; Tanner, T. F. N.; Whitwood, A. C.; Clark, I. P.; Towrie, M.; Krieger, J. P.; Lynam, J. M.; Fairlamb, I. J. S. Coumarin C-H Functionalization by Mn(I) Carbonyls: Mechanistic Insight by Ultra-Fast IR Spectroscopic Analysis. *Chem. - Eur. J.* **2023**, *29*, No. e202203038.
- (20) Hammarback, L. A.; Aucott, B. J.; Bray, J. T. W.; Clark, I. P.; Towrie, M.; Robinson, A.; Fairlamb, I. J. S.; Lynam, J. M. Direct Observation of the Microscopic Reverse of the Ubiquitous Concerted Metalation Deprotonation Step in C-H Bond Activation Catalysis. *J. Am. Chem. Soc.* **2021**, *143*, 1356–1364.
- (21) Khalil, M.; Demirdöven, N.; Tokmakoff, A. Vibrational coherence transfer characterized with Fourier-transform 2D IR spectroscopy. *J. Chem. Phys.* **2004**, *121*, 362–373.
- (22) Khalil, M.; Demirdöven, N.; Tokmakoff, A. Coherent 2D IR spectroscopy: Molecular structure and dynamics in solution. *J. Phys. Chem. A* **2003**, *107*, 5258–5279.
- (23) Rector, K. D.; Kwok, A. S.; Ferrante, C.; Tokmakoff, A.; Rella, C. W.; Fayer, M. D. Vibrational anharmonicity and multilevel vibrational dephasing from vibrational echo beats. *J. Chem. Phys.* **1997**, *106*, 10027–10036.
- (24) Kiefer, L. M.; Kubarych, K. J. Two-dimensional infrared spectroscopy of coordination complexes: From solvent dynamics to photocatalysis. *Coord. Chem. Rev.* **2018**, *372*, 153–178.
- (25) King, J. T.; Baiz, C. R.; Kubarych, K. J. Solvent-dependent spectral diffusion in a hydrogen bonded “vibrational aggregate”. *J. Phys. Chem. A* **2010**, *114*, 10590–10604.
- (26) Baiz, C. R.; McCanne, R.; Nee, M. J.; Kubarych, K. J. Orientational dynamics of transient molecules measured by non-equilibrium two-dimensional infrared spectroscopy. *J. Phys. Chem. A* **2009**, *113*, 8907–8916.
- (27) Nee, M. J.; Baiz, C. R.; Anna, J. M.; McCanne, R.; Kubarych, K. J. Multilevel vibrational coherence transfer and wavepacket dynamics probed with multidimensional IR spectroscopy. *J. Chem. Phys.* **2008**, *129*, No. 084503.
- (28) Bonner, G. M.; Ridley, A. R.; Ibrahim, S. K.; Pickett, C. J.; Hunt, N. T. Probing the effect of the solution environment on the vibrational dynamics of an enzyme model system with ultrafast 2D-IR spectroscopy. *Faraday Discuss.* **2010**, *145*, 429–442.
- (29) Delor, M.; Sazanovich, I. V.; Towrie, M.; Spall, S. J.; Keane, T.; Blake, A. J.; Wilson, C.; Meijer, A. J.; Weinstein, J. A. Dynamics of ground and excited state vibrational relaxation and energy transfer in transition metal carbonyls. *J. Phys. Chem. B* **2014**, *118*, 11781–11791.
- (30) Cahoon, J. F.; Sawyer, K. R.; Schlegel, J. P.; Harris, C. B. Determining transition-state geometries in liquids using 2D-IR. *Science* **2008**, *319*, 1820–1823.
- (31) Baiz, C. R.; McRobbie, P. L.; Preketes, N. K.; Kubarych, K. J.; Geva, E. Two-dimensional infrared spectroscopy of dimanganese decacarbonyl and its photoproducts: an ab initio study. *J. Phys. Chem. A* **2009**, *113*, 9617–9623.
- (32) Baiz, C. R.; Nee, M. J.; McCanne, R.; Kubarych, K. J. Ultrafast nonequilibrium Fourier-transform two-dimensional infrared spectroscopy. *Opt. Lett.* **2008**, *33*, 2533–2535.
- (33) Oppelt, K.; Mosberger, M.; Ruf, J.; Fernández-Terán, R.; Probst, B.; Alberto, R.; Hamm, P. Shedding Light on the Molecular Surface Assembly at the Nanoscale Level: Dynamics of a Re(I) Carbonyl Photosensitizer with a Coadsorbed Cobalt Tetrapyrrolyl Water Reduction Catalyst on ZrO<sub>2</sub>. *J. Phys. Chem. C* **2020**, *124*, 12502–12511.
- (34) Stewart, A. I.; Wright, J. A.; Greetham, G. M.; Kaziannis, S.; Santabarbara, S.; Towrie, M.; Parker, A. W.; Pickett, C. J.; Hunt, N. T. Determination of the photolysis products of [FeFe]hydrogenase

enzyme model systems using ultrafast multidimensional infrared spectroscopy. *Inorg. Chem.* **2010**, *49*, 9563–9573.

(35) Horch, M.; Schoknecht, J.; Wrathall, S. L. D.; Greetham, G. M.; Lenz, O.; Hunt, N. T. Understanding the structure and dynamics of hydrogenases by ultrafast and two-dimensional infrared spectroscopy. *Chem. Sci.* **2019**, *10*, 8981–8989.

(36) Kulka-Peschke, C. J.; Schulz, A. C.; Lorent, C.; Rippers, Y.; Wahlefeld, S.; Preissler, J.; Schulz, C.; Wiemann, C.; Bernitzky, C. C. M.; Karafoulidi-Retsou, C.; Wrathall, S. L. D.; Procacci, B.; Matsuura, H.; Greetham, G. M.; Teutloff, C.; Lauterbach, L.; Higuchi, Y.; Ishii, M.; Hunt, N. T.; Lenz, O.; Zebger, I.; Horch, M. Reversible Glutamate Coordination to High-Valent Nickel Protects the Active Site of a [NiFe] Hydrogenase from Oxygen. *J. Am. Chem. Soc.* **2022**, *144*, 17022–17032.

(37) Wrathall, S. L. D.; Procacci, B.; Horch, M.; Saxton, E.; Furlan, C.; Walton, J.; Rippers, Y.; Blaza, J. N.; Greetham, G. M.; Towrie, M.; Parker, A. W.; Lynam, J.; Parkin, A.; Hunt, N. T. Ultrafast 2D-IR spectroscopy of [NiFe] hydrogenase from *E. coli* reveals the role of the protein scaffold in controlling the active site environment. *Phys. Chem. Chem. Phys.* **2022**, *24*, 24767–24783.

(38) Procacci, B.; Wrathall, S. L. D.; Farmer, A. L.; Shaw, D. J.; Greetham, G. M.; Parker, A. W.; Rippers, Y.; Horch, M.; Lynam, J. M.; Hunt, N. T. Understanding the [NiFe] Hydrogenase Active Site Environment through Ultrafast Infrared and 2D-IR Spectroscopy of the Subsite Analogue K[CpFe(CO)(CN)<sub>2</sub>] in Polar and Protic Solvents. *J. Phys. Chem. B* **2024**, *128*, 1461–1472.

(39) Ward, J. S.; Lynam, J. M.; Moir, J. W.; Sanin, D. E.; Mountford, A. P.; Fairlamb, I. J. A therapeutically viable photo-activated manganese-based CO-releasing molecule (photo-CO-RM). *Dalton Trans.* **2012**, *41*, 10514–10517.

(40) Deflores, L. P.; Nicodemus, R. A.; Tokmakoff, A. Two-dimensional Fourier transform spectroscopy in the pump-probe geometry. *Opt. Lett.* **2007**, *32*, 2966–2968.

(41) Shim, S. H.; Zanni, M. T. How to turn your pump-probe instrument into a multidimensional spectrometer: 2D IR and Vis spectroscopies via pulse shaping. *Phys. Chem. Chem. Phys.* **2009**, *11*, 748–761.

(42) Hamm, P.; Zanni, M. *Concepts and Methods of 2D Infrared Spectroscopy*; Cambridge University Press, 2011.

(43) Frisch, M. J.; Trucks, G. W.; Schlegel, H. B.; Scuseria, G. E.; Robb, M. A.; Cheeseman, J. R.; Scalmani, G.; Barone, V.; Petersson, G. A.; Nakatsuji, H.; Li, X.; Caricato, M.; Marenich, A. V.; Bloino, J.; Janesko, B. G.; Gomperts, R.; Mennucci, B.; Hratchian, H. P.; Ortiz, J. V.; Izmaylov, A. F.; Sonnenberg, J. L.; Williams, F.; Lipparini, F.; Egidi, F.; Goings, J.; Peng, B.; Petrone, A.; Henderson, T.; Ranasinghe, D.; Zakrzewski, V. G.; Gao, J.; Rega, N.; Zheng, G.; Liang, W.; Hada, M.; Ehara, M.; Toyota, K.; Fukuda, R.; Hasegawa, J.; Ishida, M.; Nakajima, T.; Honda, Y.; Kitao, O.; Nakai, H.; Vreven, T.; Throssell, K.; Montgomery, J. A., Jr.; Peralta, J. E.; Ogliaro, F.; Bearpark, M. J.; Heyd, J. J.; Brothers, E. N.; Kudin, K. N.; Staroverov, V. N.; Keith, T. A.; Kobayashi, R.; Normand, J.; Raghavachari, K.; Rendell, A. P.; Burant, J. C.; Iyengar, S. S.; Tomasi, J.; Cossi, M.; Millam, J. M.; Klene, M.; Adamo, C.; Cammi, R.; Ochterski, J. W.; Martin, R. L.; Morokuma, K.; Farkas, O.; Foresman, J. B.; Fox, D. J. *Gaussian 16*, Rev. C.02; Gaussian Inc.: Wallingford, CT, 2016.

(44) Farrell, I. R.; Matousek, P.; Towrie, M.; Parker, A. W.; Grills, D. C.; George, M. W.; Vlcek, A., Jr. Direct observation of competitive ultrafast CO dissociation and relaxation of an MLCT excited state: picosecond time-resolved infrared spectroscopic study of [Cr(CO)<sub>4</sub>(2,2'-bipyridine)]. *Inorg. Chem.* **2002**, *41*, 4318–4323.

(45) Bernhard, S.; Omberg, K. M.; Strouse, G. F.; Schoonover, J. R. Time-resolved IR studies of [Re(LL)(CO)<sub>4</sub>]<sup>+</sup>. *Inorg. Chem.* **2000**, *39*, 3107–3110.

(46) Kania, R.; Stewart, A. I.; Clark, I. P.; Greetham, G. M.; Parker, A. W.; Towrie, M.; Hunt, N. T. Investigating the vibrational dynamics of a 17e(−) metalcarbonyl intermediate using ultrafast two dimensional infrared spectroscopy. *Phys. Chem. Chem. Phys.* **2010**, *12*, 1051–1063.

(47) Banno, M.; Iwata, K.; Hamaguchi, H. O. Intermolecular interaction between W(CO)<sub>6</sub> and alkane molecules probed by ultrafast

vibrational energy relaxation: anomalously strong interaction between W(CO)<sub>6</sub> and decane. *J. Phys. Chem. A* **2009**, *113*, 1007–1011.

(48) Arrivo, S. M.; Dougherty, T. P.; Grubbs, W. T.; Heilweil, E. J. Ultrafast Infrared-Spectroscopy of Vibrational CO-Stretch up-Pumping and Relaxation Dynamics of W(CO)<sub>6</sub>. *Chem. Phys. Lett.* **1995**, *235*, 247–254.

(49) Kenkre, V. M.; Tokmakoff, A.; Fayer, M. D. Theory of Vibrational-Relaxation of Polyatomic-Molecules in Liquids. *J. Chem. Phys.* **1994**, *101*, 10618–10629.

(50) Tokmakoff, A.; Sauter, B.; Fayer, M. D. Temperature-Dependent Vibrational-Relaxation in Polyatomic Liquids - Picosecond Infrared Pump-Probe Experiments. *J. Chem. Phys.* **1994**, *100*, 9035–9043.

(51) Moore, P.; Tokmakoff, A.; Keyes, T.; Fayer, M. D. The Low-Frequency Density-of-States and Vibrational Population-Dynamics of Polyatomic-Molecules in Liquids. *J. Chem. Phys.* **1995**, *103*, 3325–3334.

(52) Crum, V. F.; Kiefer, L. M.; Kubarych, K. J. Ultrafast vibrational dynamics of a solute correlates with dynamics of the solvent. *J. Chem. Phys.* **2021**, *155*, No. 134502.

(53) Zális, S.; Farrell, I. R.; Vlcek, A. The involvement of metal-to-CO charge transfer and ligand-field excited states in the spectroscopy and photochemistry of mixed-ligand metal carbonyls: A theoretical and spectroscopic study of [W(CO)<sub>4</sub>(1,2-ethylenediamine)] and [W(CO)<sub>4</sub>(N,N'-bis-alkyl-1,4-diazabutadiene)]. *J. Am. Chem. Soc.* **2003**, *125*, 4580–4592.

(54) Guillaumont, D.; Vlcek, A.; Daniel, C. Photoreactivity of Cr(CO)<sub>4</sub>(2,2'-bipyridine): Quantum chemistry and photodissociation dynamics. *J. Phys. Chem. A* **2001**, *105*, 1107–1114.

(55) Stewart, A. I.; Clark, I. P.; Towrie, M.; Ibrahim, S. K.; Parker, A. W.; Pickett, C. J.; Hunt, N. T. Structure and vibrational dynamics of model compounds of the [FeFe]-hydrogenase enzyme system via ultrafast two-dimensional infrared spectroscopy. *J. Phys. Chem. B* **2008**, *112*, 10023–10032.